The seismic velocity and fault structure of the Erzincan basin, Turkey, using local earthquake tomography

M. Aktar,[1,3] C. Dorbath[2] and E. Arpat[1]

[1]*Bogazici University, Kandilli Observatory and Earthquake Research Institute, Cengelkoy* 81220, *Istanbul, Turkey. E-mail: aktar@boun.edu.tr*
[2]*Institut de Physique du Globe de Strasbourg, 5 rue Rene Descartes,* 67084 *Strasbourg, Cedex, France*
[3]*TUBITAK, Marmara Research Centre, Institute of Earth and Marine Sciences, Gebze* 41470, *Kocaeli, Turkey*

SUMMARY
We present a detailed 3-D seismic velocity model for the upper crust, beneath the Erzincan Basin using tomographic inversion applied to the bodywave arrivals of the 1992 March 13 Erzincan earthquake ($M_l = 6.9$) aftershock sequence. High quality digital data collected by various institutions is used, consisting of 1240 hypocentres with rms errors less than 0.10 s, recorded by 25 stations on average. This provides a total of approximately 21 000 *P*- and 10 000 *S*-arrival times. The final solution is well constrained and reveals sharp boundaries bordering the basin. The shape of the basin is found to be deeper on the north and narrower at the eastern border. The velocity contrast related to the basin extends down to a depth of 3 km, but is hardly perceptible at 6 km and completely disappears at 9 km. The thickness of low-velocity unconsolidated soft sediments ($V_p < 2000$ m s^{-1}) is estimated to be shallower than 3 km. The hypocentres were relocated using the inferred 3-D model and correlated with the fault segments that were observed in field studies. In addition to the main segment of the North Anatolian Fault (NAF), on the north of the basin, we identified a secondary faulted zone located along the southern border of the basin and merging with the Pulumur Fault Zone. We observed that this southern zone has a limited extension towards east (∼20 km) and therefore played only a minor role in the evolution of the basin. Despite the complex interaction between the North Anatolian Fault, the Ovacık Fault and the Pulumur Fault Zone, it is clear that the Erzincan Basin has developed predominantly by the pull-apart mechanism. We conclude that the main continuation of NAF to the east is the branch on the north following the Euphrates valley, and constitutes, locally, the primary seismic hazard factor.

Key words: aftershocks, tomography.

GJI Seismology

1 INTRODUCTION

Eastern Turkey is located in a north–south converging collision zone between the Eurasian Plate to the north and the Arabian Plate to the south. Between these two plates lies the Anatolian microplate, which, due to the north–south compression, is being forced westward along two major strike-slip faults, namely the North Anatolian Fault (NAF) and the East Anatolian Fault (EAF) (Şengör *et al.* 1985; Şengör & Yilmaz 1987). The Erzincan Basin is one of the several pull-apart basins located along the NAF. In the last century two destructive earthquakes have occurred causing significant loss of life in the town of Erzincan: 1939 December 12, $M_s = 8.2$ (Barka & Kadinsky-Cade 1988) and 1992 March 13, $M_s = 6.8$ (Fuenzalida *et al.* 1997).

The tectonic evolution of the Erzincan Plain has been studied by a number of investigators (Hempton & Linneman 1984; Barka & Kadinsky-Cade 1988; Barka & Gülen 1989; Suzanne *et al.* 1990). The source properties of the aforementioned large events have at-

tracted considerable attention over the years, producing an abundant literature on the seismogenic characteristics of the Plain (Bernard *et al.* 1992, 1997; Barka & Eyidogan 1993; Pinar *et al.* 1994). In spite of this growing interest, the deep structure of the basin, which underlies most of the Plain, is still poorly known. Neither deep borehole data, nor seismic reflection records exist to provide a first-order estimate of the velocity distribution at depth. Previous attempts to assess the thickness of the basin fill are based on sedimentological observations and the results are often of limited precision (Hempton & Dunne 1984). Gaucher (1994) utilized *S-P* converted phases of the 1992 aftershock sequence and estimated the base of low-velocity (<2000 m s^{-1}) unconsolidated sediments, to lie between 650–2100 m depth. Recently, *S*-wave splitting analysis by Gamar & Bernard (1997) supported the existence of strong anisotropy in shallow sedimentary layers.

In this study, we present a detailed model for the *P*-wave velocity structure of the upper 9 km of the crust beneath the Erzincan Basin and surroundings. Following the 1992 March 13 earthquake

($M_l = 6.9$), which severely damaged the city of Erzincan, the aftershock activity was monitored over a period of two months. All *P*- and *S*-wave arrival times were simultaneously inverted for hypocentres and 3-D *P*-wave velocity structure. The tomographic inversion procedure applied in this study is the widely known method first introduced by Thurber (1983) and developed by Eberhart-Philips (1990) and Eberhart-Philips & Michael (1993). The damped-least-squares, full matrix inversion, iterative process is based on parametrizing the crustal structure by assigning velocity values at discrete gridpoints randomly distributed on layers inside the crust. All the remaining velocity values that are between the gridpoints are deduced by linear interpolation. An approximate ray tracing algorithm (ART, Thurber 1983) is used to calculate traveltime between the source and the station. This code was developed for regions where events occur within the target area and is often used for earthquake source regions and aftershocks studies. We obtained a well-resolved 3-D velocity structure down to a depth of 9 km, which is the first detailed model to be proposed for the Erzincan basin. The final location of the hypocentres after inversion allowed a better assessment of the aftershock activity, which is correlated with surface faults that were mapped by aerial photography and field observations.

2 GEOLOGICAL AND TECTONICAL SETTING

The tectonic structure of the Erzincan Basin reflects a complex geodynamic regime in which the major geological features are a consequence of the relative plate motion between the Eurasian Plate (Pontides on the north) and Anatolian Plate (the Taurides on the south). The NAF is an east west oriented right lateral strike-slip system, which defines the plate boundary and takes up the major part of the plate motion. The Erzincan Basin is one the several moderate size (40 × 12 km²) Cenozoic basins that formed along the NAF. The structural units located around the basin generally mark an east west trend and strongly reflect the transform tectonic associated the NAF. The geological units on the north of the basin are the serpentinized peridotites of Kesis Mountain (3549 m) and on the south,

the Upper Triassic to Lower Cretaceous limestone of Munzur Mountain (3463 m) (Fig. 1) (Ozgul & Tursucu 1984; Westaway & Arger 2001). Younger sedimentary deposits also occupy a significant part of the local geology and reach up to an altitude of 2800 m on both sides of the basin. Lower Miocene deposits include recifal limestone, marls, green clay and coal seams. Upper Miocene sequences consist of evaporites and fluvial deposits reaching considerable thickness at some locations. All the units described above are bounded by ancient inactive thrust faults, forming roughly east–west trending slices. Both pre- and post-Miocene rocks are strongly folded and fractured due the compressional tectonics. Barka & Gülen (1989) argued that the south-dipping thrust faults are developed by the reactivation of older normal faults, which once marked the borders of the Miocene basins. The central and eastern section of the basin has a flat topography and constitutes the main depositional setting for the alluvium of the Euphrates River. The western part is dominated by gentle slopes of alluvial fans formed by sediment flux originating from the secondary streams draining the northwestern rim of the depression. Several dacitic–rhyolitic volcanic domes are aligned along the northern border (Fig. 2) and date between 0.25–3.1 Ma (Hempton & Linneman 1984).

Mapped surficial faults within the Erzincan Basin strike roughly NW–SE, paralleling the northern margin of the basin and can be clearly identified as the active segment of the NAF. 7 km to the east of Erzincan, the NAF zone consists of a series of four subparallel faults having a total length of 22 km and an average strike of N133°. Along this section of the fault lie most of the volcanic domes. At the eastern end of the basin, the main segment of the NAF strikes eastward (N113°) along the narrow gorges of Euphrates for approximately 10 km, then joins yet another segment with a minor change in strike (N106°) and extends up to Yedisu Plain situated 85 km WSW of Erzincan. Southeast of the basin, aerial photography and surface studies reveal a secondary group of faults, which are shown in Fig. 1. They are parallel to the southern flank of the Erzincan Basin and extend to the city of Pulumur, situated 45 km SE from Erzincan. This fault zone, also of late Quaternary age, is composed of several short segments, the majority having a strike-slip character parallel to the
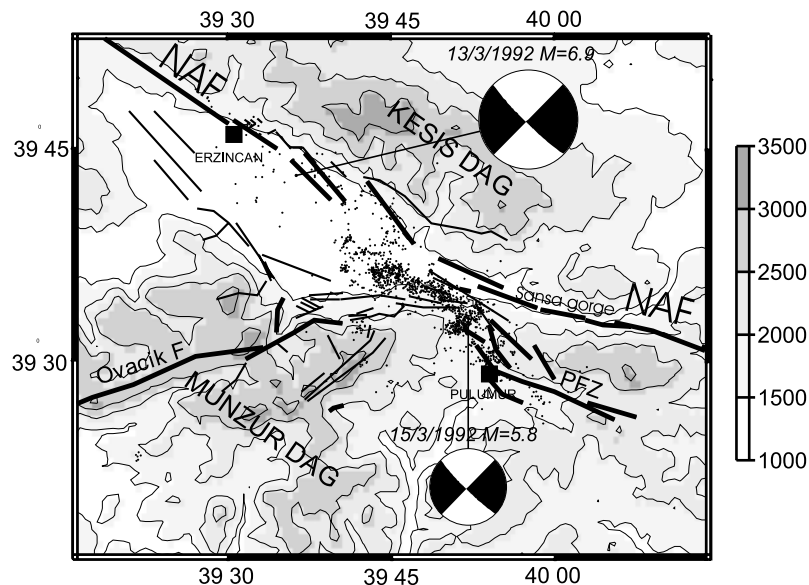

Figure 1. Topographic map of the Erzincan Basin and surroundings, with the main structural units: NAF, PFZ and the major mountain ranges. The location and source mechanism for the mainshock of 1992 March 13 ($M_l = 6.9$) and the largest aftershock (1992 March 15 $M_l = 5.8$), the location of aftershocks used in this study are also given. Elevations are in metres.
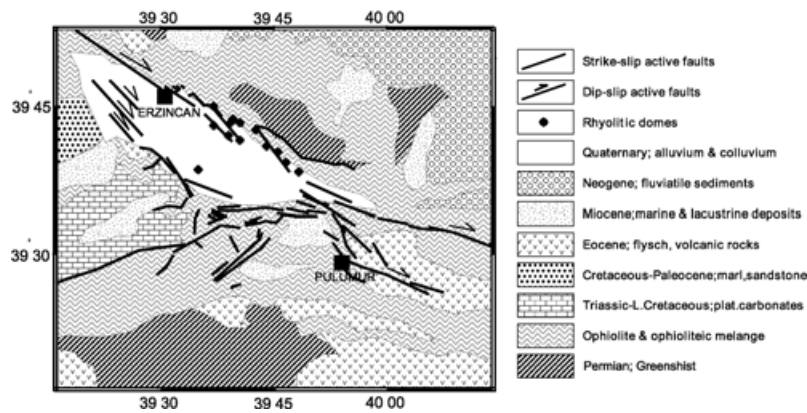
Figure 2. Geological map of the Erzincan Basin and surroundings. Thick solid segments document the faults, which were identified as right lateral strike slip from geomorphology evidence. Volcanic domes scattered on the border of the basin are also shown (solid circles).

main segment of the NAF. The surface features associated with this prominent southern branch can be followed for another 20 km to the southeast of Pulumur where, eventually, no further surface expression can be seen. This last section runs into an ophiolitic melange and is not well studied. The largest aftershock (1992 March 15 M_l = 5.8) following the mainshock of 1992 is located in this southern zone, which we call the Pulumur Fault Zone (PFZ). Finally, the Ovacik Fault (OF, Arpat & Saroglu 1975), which joins the Erzincan Basin tangentially from the southeast, is also an influence on the structure and contributes to the morphogenesis of the Erzincan Basin. The merging point of OF with PFZ and eventually with the main branch of NAF, strongly contributes to the complexity of the southern border of the Erzincan Basin. A number of faults of different character are identified in this zone, lying between NAF and PFZ. The majority have a dominant dip-slip component with only one exception, which shows a definite strike-slip character in the direction of N135°. Most of the prominent normal faults are located on the southeastern sector of the basin where larger fault planes dip northward, towards the basin, and the lesser antithetic faults dip southwards, towards the Munzur Mountains (Fig. 2). The alluvium-covered central part of the basin shows no morphological evidence of active faults although one would naturally expect their existence. In this area high deposition rates from the Euphrates River and intensive agricultural activity are not favourable to the preservation of relatively young fault scarps.

3 DATA AND METHODS

The traveltime data used in the tomographic inversion were collected during the aftershock activity following the 1992 Erzincan Earthquake. Three different institutions were independently involved in the data collection process: Ecole et Observatoire des Sciences de la Terre de Physique du Globe de Strasbourg, France (Fuenzalida *et al.* 1997), Geoforschung Zentrum of Potsdam, Germany (Baumbach *et al.* 1994) and Marmara Research Centre of TUBITAK, Turkey (Aktar *et al.* 1996). Data were recorded on digital Reftek 72A-06 and analogue Geophon data recorders for a total of 72 stations. The latter were digitized offline. GPS, Omega and DCF were used for timing synchronization with an accuracy of ±10 ms or less. Over 2000 events were recorded in a period of 2 months. The readings from the three groups were merged to obtain a single comprehensive data set, which, in turn, was passed through a selection process. Since the majority of the seismometers were short period vertical velocity sensors, we have considered only the *P*-

velocity model. The *S*-velocity model had a very low resolution due to the small quantity and low quality of *S*-phase readings and therefore was not considered in this study. However, the available *S*-arrival data were used in the location process during the inversion because they provided additional constraints for the hypocentral depths. The *S* velocities were directly obtained from the *P* velocities, assuming an *a priori* known V_p/V_s ratio of 2.4 for the upper 3 km as implied by Gaucher (1994) and 1.79 for the deeper layers.

The events that were used in this tomographic inversion were all recorded during a period starting 10 d after the mainshock. We note that the majority of aftershocks are clustered in the southeast Erzincan Basin, considerably distant from (>30 km SE) the mainshock, but closer (<10 km) to the strong Pulumur aftershock. The earlier aftershocks may possibly have been located nearer to the mainshock along the main branch of the NAF (Aktar *et al.* 1996).

A conservative selection and elimination was done in order to obtain a more reliable and uniform data quality. The selection process was applied after an initial location of the hypocentres with HYPOINVERSE (Klein 1978) using the optimal 1-D crustal structure proposed by Fuenzalida *et al.* (1997). Following the initial location of the events, all hypocentres that did not satisfy a predetermined quality criterion were discarded for the remaining part of the study. Only events registered by more than 10 stations, having a root mean square (rms) error of less than 0.25 s, and a conditioning factor of less than 100 for the Geiger matrix were kept. The number of events is reduced to 1240 hypocentres with rms error <0.10 s and recorded by 25 stations on average. This provided a total of approximately 21 000 *P*- and 10 000 *S*-arrival times.

The tomographic inversion was applied over an area of 80 × 60 km². The average distance between the gridpoints is 5 km in the centre of the network and 10 km around the peripheries (Fig. 3). The 3 km vertically spaced partitioning is restricted to the upper 9 km since most hypocentres are located in the upper 10 km of the crust. The E–W and N–S velocity grid orientation is independent of the regional geological structural trend. Test inversions were done by taking the grid axis parallel to the direction of the NAF (i.e. N133°) and the results did not show any significant differences.

The standard approach in the implementation of the tomographic inversion is to start the iteration with an estimated optimal 1-D crustal model. Methods based on the simultaneous inversion of the hypocentre and crustal model such as VELEST (Kissling 1988; Kissling *et al.* 1994) are often used to determine the best initial model for the inversion procedure. However, in this example the optimal
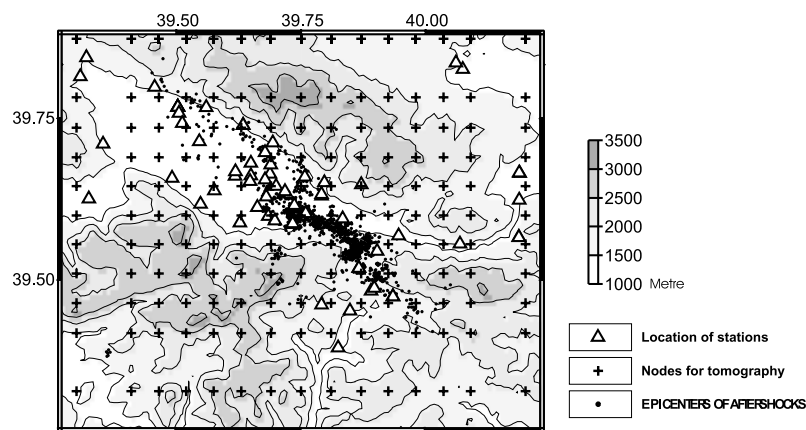
Figure 3. Map of the Erzincan Basin and surroundings, with the location of aftershocks (filled curves), seismic stations (triangles) and the nodes used in the tomographic inversion (cross).

1-D model obtained by VELEST did not prove to be a suitable choice as an initial model for starting the tomographic iteration. This is most likely to be due to the existence of the strong lateral variations in the crustal structure particularly in the 3 km upper layer, caused mainly by the soft sediments of Erzincan basin embanked between the mountains. An educated guess was therefore made taking into account the low-velocity alluvial basin. This initial model produced a fast and reliable solution convergence. The mapview of P-wave velocity distribution at various depths is given in Fig. 4.

As Thurber's method uses damped least-squares inversion, we constructed trade-off curves of resolution against solution error to select the optimal value of the damping factor. The value of 35 was finally selected, which allows a good resolution with errors lower than 0.1 km s^{-1} for P-wave velocities. Besides the rotation of the grid, we tested the stability of the inversion by altering the horizontal and vertical spacing of the gridpoints. The resulting velocity changes fell within the original velocity model errors and gave us confidence in the stability of the solution.

Moreover, the quality of the inversion is illustrated by the values of the diagonal elements of the resolution matrix (Fig. 5), as the standard approach in most tomographic inversions (Kissling 1988; Hauksson & Haase 1997). In the resolution matrix, the values of the off-diagonal elements indicate the degree of coupling between neighbouring nodes, and consequently it is desirable to have the resolution matrix close to the identity matrix, which would mean that the solution is perfectly resolved. In our case, due to the very good source station distribution and the very high number of intersecting rays, the values of the diagonal elements are generally above 0.5 in most of the central part of the grid. The nodes at the surface layer, which have the highest resolution values, naturally correspond to the location of the seismic stations. The highest resolution values are obtained for the depths of 3 and 6 km, up to 0.85 in the centre of the model that is the best sampled by rays. At 9 km depth, the values decrease due to the low number of deep events. The processing time involved in the inversion process is significant considering the number of stations and the number of events involved. The inversion process is repeated until a satisfactory improvement in the residuals is obtained and the 3-D crustal model settles to a stable value. The initial P data variance was 0.054 s^2, after six iterations a reduction of 74 per cent is achieved with the final variance of 0.014 s^2.

4 RESULTS

4.1 Hypocentre location

The comparison of the initial hypocentre location and the final location obtained through inversion shows significant improvement by the use of the tomographic approach. The reduction in the hypocentre scattering is clearly illustrated by plotting the correction vectors both in the horizontal and vertical (Fig. 6). The map view of the correction vectors shows clearly that the correction becomes more significant as the hypocentre is located further away from the centre of the basin where the seismic network is located. Hypocentres located inside the basin are not significantly influenced by the tomographic inversion since the initial 1-D model was chosen to take into account the effect of the sedimentary basin. Hypocentres previously located outside the basin relocated nearer the centre of the Plain. The events previously distributed randomly in the northeast were displaced 4–8 km to the southeast aligning along a section of the NAF, which presumably ruptured in 1939. Similarly, in the southeast side of the basin, events scattered in the mountainous zone of Pulumur shifted 4–6 km to the northwest, forming a cluster in a narrow complex strip along the southern border of the Erzincan Basin, where the OF joins the NAF zone. The use of the 3-D crustal model leads also to significant improvements in the vertical distribution of the hypocentres. The extent of this improvement is illustrated in two vertical cross-sections, one parallel (Fig. 6, section AA′) and one normal (Fig. 6, section BB′) to the strike direction of the NAF. In section (AA′) events previously located below 10 km have changed from 3 to 6 km to shallower depths. In the upper 4 km many events became deeper by 2–4 km depth. The overall effect of the 3-D modelling in depth distribution of the hypocentres was to constrain the total aftershock activity within a well-defined seismogenic zone, which roughly lies between 4–11 km. The cross-section taken normal to the fault plane (Fig. 6c, section BB′) illustrates clearly the distinction that exists between the activity in the northern and southern margins of the basin. The 3-D modelling suitably modified the location of the hypocentres both in the vertical and horizontal directions, such that the events cluster around two separate vertical lines. These may represent the narrow post-seismic stress release zones about two prominent fault planes of the NAF and the PFZ.
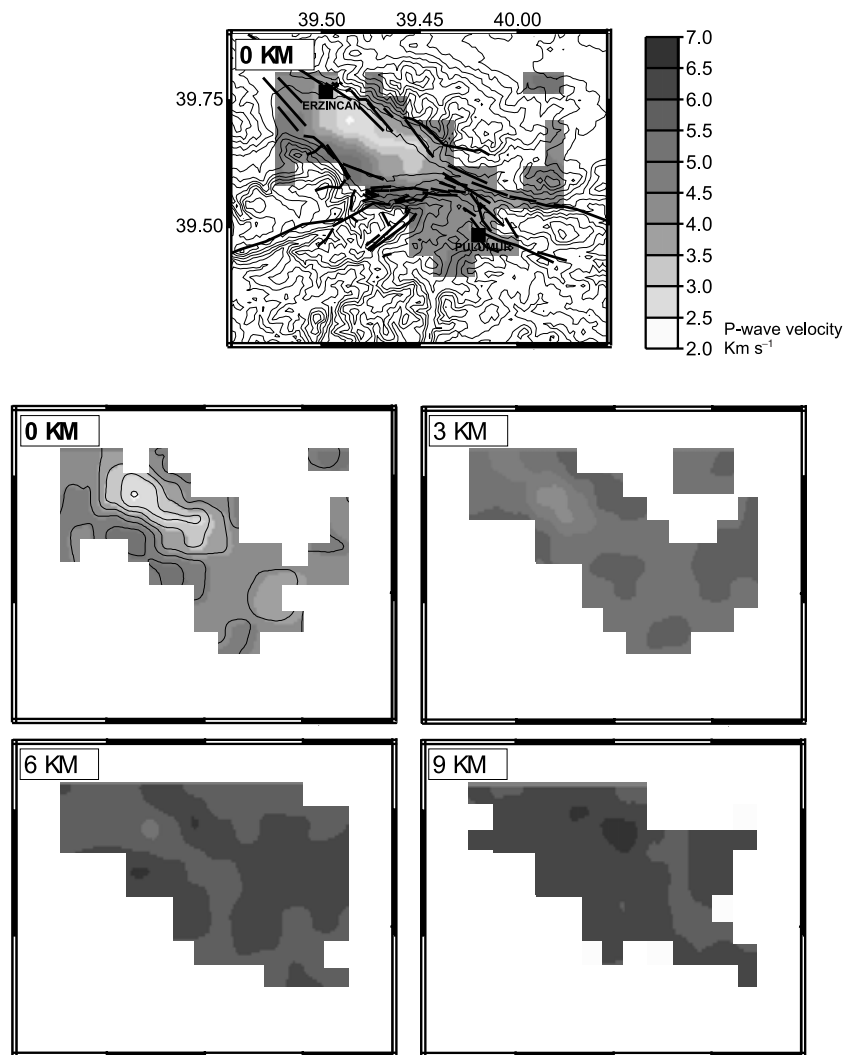
Figure 4. Shaded view of the *P*-velocity distribution at the surface layer superimposed with topographic contours and major faults. The contour map of *Pn* velocities at various depths (0, 3, 6 and 9 km) beneath the Erzincan Basin and surroundings.

The hypocentres are aligned vertically along both the northern and southern sides of the basin pointing to the existence of two distinct weakness zones (Fig. 7 section BB′). Hypocentres located along the northern border of the basin, coincide with the main rupture plane of the NAF while the southern ones are aligned along older fault traces, which, in the east, joins the PFZ. The aftershock activity gradually switches from the northern to the southern zone at the east of the basin. The main branch of the NAF, which follows the Sansa Gorge on the north, is totally exempt from any aftershock activity and all hypocentres are confined within the plane of weakness representing the PFZ (Fig. 7 section DD′).

In a previous paper, Fuenzalida *et al.* (1997) analysed the aftershocks recorded by the French temporary network. These authors, in order to account for the assumed velocity variations between the basin and the adjacent mountains, computed station corrections. Doing so, they reduced the initial scatter of the crude HYPOINVERSE results, which do not take into account the possible low velocities in the basin. It is satisfying to note that the overall picture of the aftershocks distribution that we obtain by tomographic inversion is very similar to that presented in their paper. Indeed, a station correction is a simple way to account for the local variations of the 3-D

velocity, with respect to the mean 1-D velocity model used in simple HYPOINVERSE application.

4.2 Velocity structure

The tomographic solution for the velocity structure is sufficiently constrained and the variation of V_p with depth illuminates the basin shape, the basement structure and the structure beneath the surrounding mountain ranges. Large *P*-wave velocity variations were found in the surface layer, which correlate well with the morphological features at the surface (Fig. 4). The effect of alluvial fill in the basin is reflected in a most striking way by the strongly marked low V_p corridor lying in the NE–SW direction, parallel to the northern edge of the basin. The lowest V_p values (1.6 km s^{-1}) are due to the unconsolidated sedimentary deposits, which are expected to fill the upper 1–1.5 km of the basin. The low surface velocities terminate in the southwest in a zone of intense aftershock activity where the basin meets the mountains. This corresponds to the PFZ where the strong aftershock of 15 March is located (Fuenzalida *et al.* 1997). Relatively high-velocity values ($V_p \geq 5.5$ km s^{-1}) were observed beneath deep-rooted structural units such as the Munzur Mountain
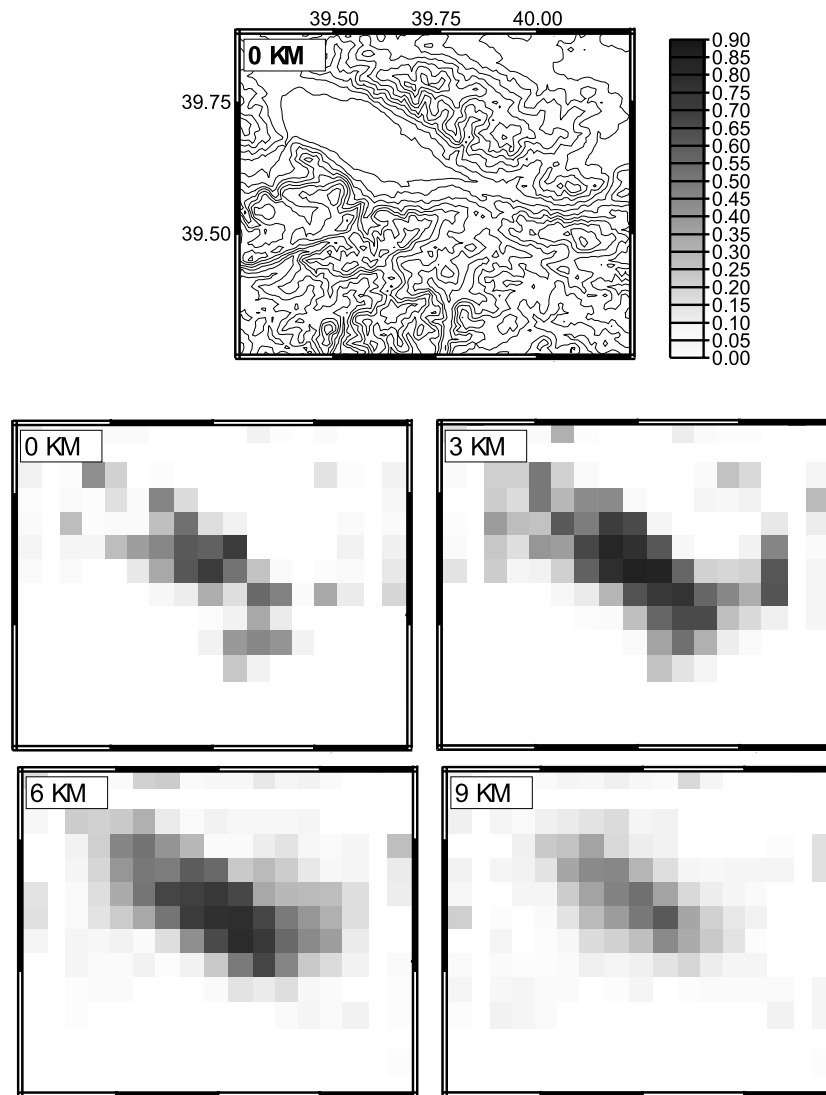
Figure 5. Shaded view of the resolution matrix corresponding to *P* velocities given by tomographic inversion, obtained for various depth levels beneath the Erzincan Basin.

Ranges, which form the southern border of the Erzincan Basin. We note that peridotite blocks are among the main constituents of the melange that forms the mountains surrounding the Erzincan basin. In contrast to the above-mentioned major structural units, there is no indication of any velocity variation due to the presence of the volcanic outlets, which are aligned along the northern border of the basin. We suggest that potential velocity anomalies from structures connecting the volcanic chimneys to deeper layers are below the resolving power of our tomographic inversion. The layer with nodes at 3 km depth, has lateral V_p variations similar to the surface layer, but less pronounced with velocities ranging from 3.2 to 5.0 km s^{-1} (Fig. 4b). A minimum value of 3.2 km s^{-1} is reached at a location near the northeastern flank of the basin and indicates its deepest part.

The velocity structures at 6 and 9 km layers (Figs 4c and d) are totally distinct in character from the two shallower ones. The nodes at these depths are located inside the zone where the aftershock activity is concentrated. The velocity distribution is more homogeneous and the lateral variation of the velocity appears to be completely uncorrelated with surface structures. *P*-wave velocities

range from 5.5 to 6.4 km s^{-1}. Diffuse patterns of low velocities can still be seen at 6 km below the basin, but disappear completely at a depth of 9 km.

The depth sections taken normal to the NAF clearly show the distribution of the aftershocks with respect to the borders of the basin (Fig. 7). The section AA′ corresponds to the northeast limit of the basin and includes the deepest part of the basin morphology. Sedimentary velocities in the basin range from 1.6 to 4.5 km s^{-1} and extend to a depth of 4–6 km. The high V_p values at the deeper section (5–8 km) of the basin represent a sediment-bedrock transition zone. We do not expect to find the unconsolidated soft sediments at such great depths, as suggested by the higher V_p values (>5.5 km s^{-1}) calculated at 6 km. Instead, we expect that the older and deeper basin units may have high levels of compaction and therefore have significant vertical velocity gradients. Basin depths found in this study are common as compared with other major transform fault systems. Tomographic studies of the Los Angeles basin on The San Andreas Fault reveal depths of 8–12 km (Hauksson & Haase 1997).

We note that, towards the east, although the surface area of the basin remains basically the same, the deeper part is much less
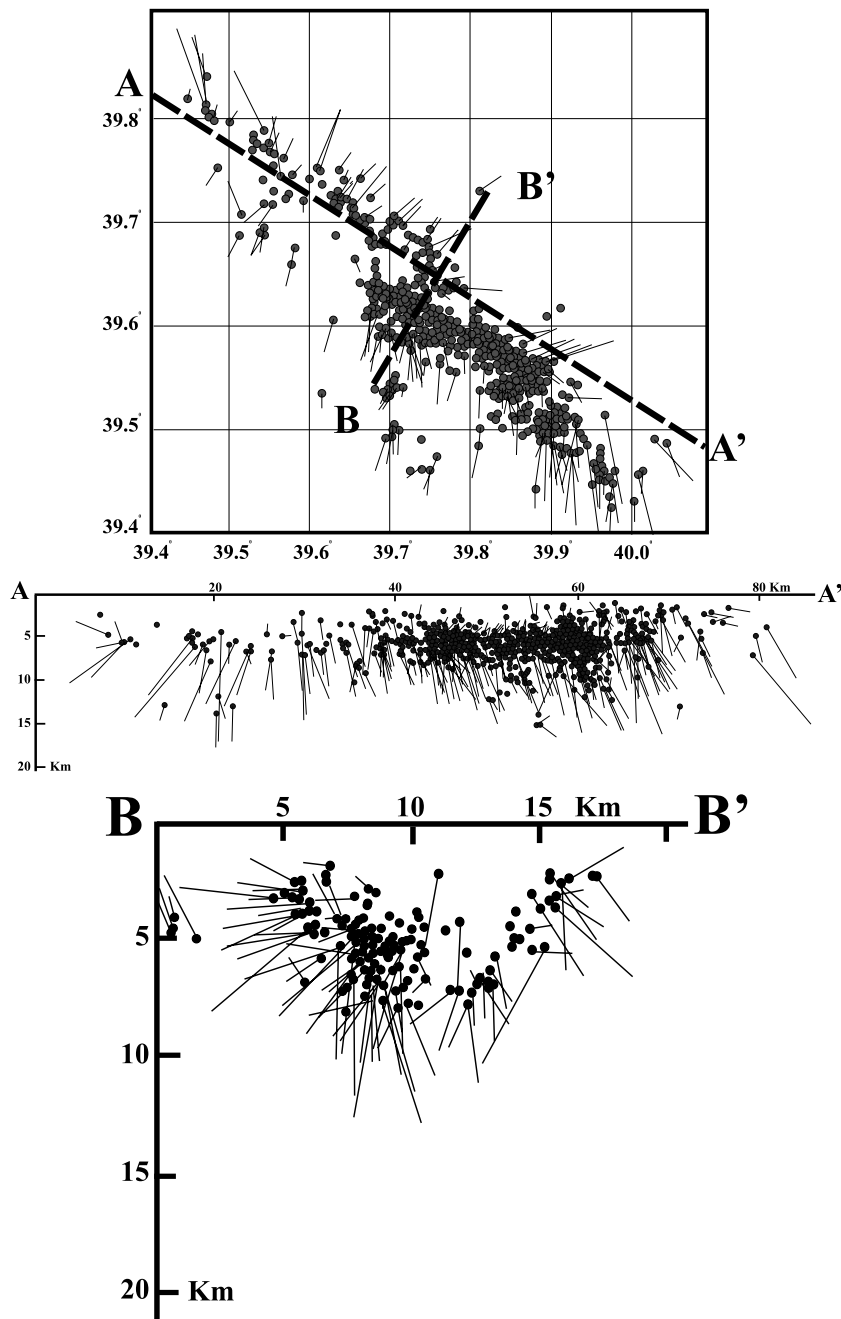
Figure 6. Comparison of the location of aftershocks obtained using the simple 1-D velocity model, and the 3-D model obtained using simultaneous 3-D relocation and velocity tomography. The thin line drawn from the 1-D to the 3-D locations, solid circle showing the final location by 3-D model. (a) Horizontal, (b) vertical section, parallel to the fault (AA′), (c) vertical section, normal to the fault (BB′).

developed (Fig. 7 section BB′). From the point of view of basin evolution, we also infer that the east part of the basin is geologically younger compared with the west. The presence of numerous young normal faults in the eastern basin (Fuenzalida *et al.* 1997), also support active basin development. Further to the east, beyond the borders of the Erzincan Basin, lateral velocity anomalies are absent (Fig. 7 sections CC′ and DD′).

5 DISCUSSION AND CONCLUSION

One of the goals of this study was to accurately image the location and the shape of the seismically active zones associated with the young deforming structures. The well-recorded aftershock sequence of 1992 Erzincan earthquake provided a useful starting point for the study of seismogenic structures. The 3-D modelling effectively reduced the overall scattering of the hypocentres, and resulted in an aftershock pattern, which was more consistent with the local structures. Previous studies have identified the EW trending northern border of the Erzincan basin as being the primary active branch of the NAF (Barka & Gülen 1989). In this study, both the alignment of the aftershocks and the surface features along the southeast border of the basin emphasized the possible existence of secondary fault zones around the city of Pulumur, namely the PFZ. This zone extends approximately 20 km in the direction of N115°, to the southeast of
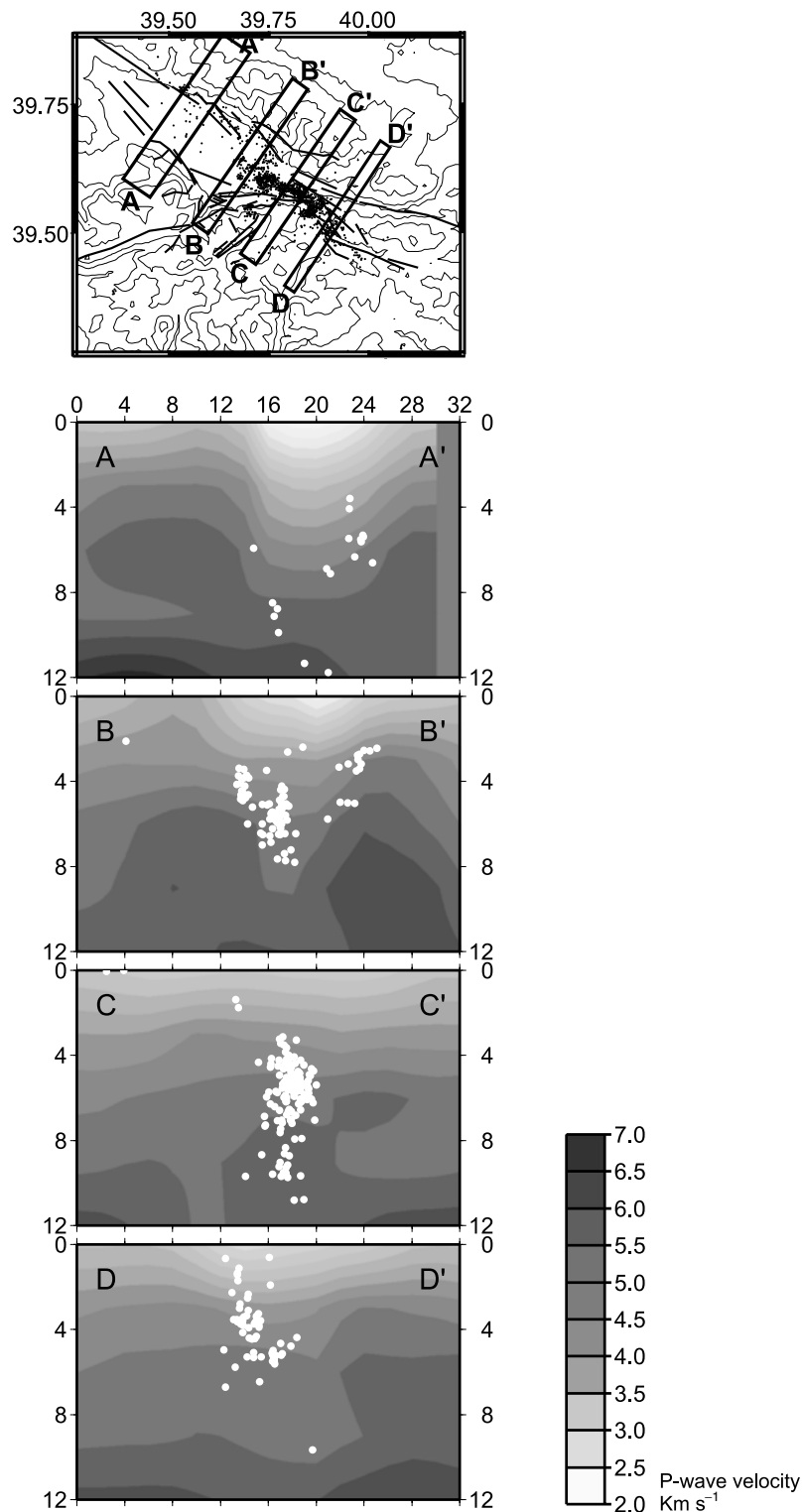
Figure 7. Cross-sections of the Erzincan Basin and surroundings, showing the velocity structure and the location of hypocentres (plain white circles). The width of the cross-sections are chosen to include a sufficient number of earthquakes to illustrate the main trend on the changing seismicity patterns.

the town of Pulumur, beyond which no trace of any continuation or any connection to other faults was detected. We conclude that PFZ, although seismically active at present time, is a secondary structure and has played a minor role in the evolution of the basin.

The upper crustal structure within the Erzincan Basin was modelled to a depth of 9 km, with sufficient accuracy allowing the imaging of large-scale basin morphology. The upper part of the crustal structure shows a striking correlation with surface features. The shape of the basin is imaged by the low-velocity corridor, which extends in the NW–SE direction, parallel to the main fault. Low-velocity basin sedimentary units are imaged to the depths of 3–4 km and the deepest point for transition to bedrock is estimated

to be at most at 6 km. The shallow part of the basin (<3 km) shows an asymmetrical cross-section with deeper part located closer to the northern border. We conclude that, at present time, the north part of the basin is subsiding faster than the south, which is expected since the active branch of the NAF is located in the north. The V_p values in deeper layers beneath the basin (>6–9 km) show very small lateral variation and correspond to average upper crustal velocities, namely 5.8–6.3 km s^{-1}.

The basin has steeply dipping walls particularly on the north side, which need to be taken into account when modelling the amplitude and the duration of the ground motion during large earthquakes. In addition to the reverberation effect in shallow sedimentary layers, laterally reflected waves may also play a major role in ground motion amplification by generating high amplitude constructive interferences (Olsen *et al.* 1995). This is particularly true in basins that have a limited lateral extent, such as the Erzincan basin and most of the other similar basins along the NAF.

We note that the V_p distribution of depth sections shows no sign of localized velocity anomalies as an evidence for any substantial basaltic/rhyolitic flow beneath the basin related to the volcanic domes. However, the resolving power of the tomography inversion may not be sufficient to track the velocity anomalies due to small-scale local structures, such as the volcanic cones scattered inside the basin.

We expect the eastern Erzincan basin to have had a highly complex evolution due to the convergence of the NAF, PFZ and the OF. A left-lateral mechanism along the OF, providing displacement of the Munzur block toward the southwest would form a suitable stress pattern for the development of normal dip-slip faults along the southern boundary. The right lateral character of the PFZ, inferred from the fault plane solutions of the aftershocks (Fuenzalida *et al.* 1997) also contributes to the extensional character by a simple a pull-apart mechanism of which the second arm would be the main branch of NAF. Despite the geometrical complexity mentioned above, it is clear that Erzincan depression has developed predominantly by pull-apart mechanism. The main continuation of the NAF to the east follows the Euphrates River, through the Sansa Gorge, and constitutes the primary seismic hazard for the area to the east of Erzincan.

ACKNOWLEDGMENTS

REFERENCES

Aktar, M., Biçmen, F., Ergin, M., Ergintav, S., Kaplan, H., Yörük, A. & Yalçın, M.N., 1996. Aftershock study of 1.10.1995 Dinar Earthquake and 13.3.1992 Erzincan Earthquake, pp. 439–448, *Proc. Earth. Symp. TUBITAK*, Pub. TUBITAK, Ankara (in Turkish).

Arpat, E. & Saroglu, F., 1975. Some recent tectonic events in Turkey, *Bull. Geol. Soc. Turkey,* **18**, 91–101.

Barka, A. & Eyidogan, H., 1993. The Erzincan Earthquake of 13 March 1992 in Eastern Turkey, *TerraNova,* **5**, 190–194.

Barka, A.A. & Gülen, L., 1989. Complex evolution of the Erzincan Basin (eastern Turkey), *J. Struct. Geol.,* **11**, 275–283.

Barka, A.A. & Kadinsky-Cade, K., 1988. Srike-slip fault geometry in Turkey and its influence in earthquake activity, *Tectonics,* **7**, 663–684.

Baumbach, M. et al, 1994. Stress redistribution during the aftershock sequence of Erzincan (Turkey) earthquake of March 13, 1992. IASPEI 27th General Assembly (Abstracts), Wellington, New Zealand.

Bernard, P., Lyon-Caen, H., Rigo, A. & Herrero, A., 1992. The Erzincan, $M = 6.8$, 1992 earthquake: analysis of near-source three component records of mainshock and aftershock, *Abstracts XXIII General Assembly of of the European Seismological Commision,* Pub. Czech. Acad. Sci., Prague.

Bernard, P., Gariel, J. & Dorbath, L., 1997. Fault location and rupture kinematics of the magnitude 6.8, 1992 Erzincan Earthquake, Turkey, from strong ground motion and regional records, *Bull. seism. Soc. Am.* **87**, 1230–1243.

Eberhart-Philips, D., 1990. Three-dimensional *P* and *S* velocity structure in the Coalinga region, California, *J. geophys. Res.*, **95**, 15 343–15 363.

Eberhart-Philips, D. & Michael, A.J., 1993. Three-dimensional velocity structure, seismicity and fault structure in the Parkfield Region, California, *J. geophys. Res.*, **98**, 15 737–15 758.

Fuenzalida, H.A., Dorbath, L., Cisternas, A., Rivera, L., Haessler, H., Philip, H., Barka, A. & Eyidogan, H., 1997. Mechanism of the 1992 Erzincan earthquake and its aftershocks, tectonics of the Erzincan basin and decoupling on the North Anatolian Fault, *Geophys. J. Int.,* **129**, 1–28.

Gamar, F. & Bernard, P., 1997. Shear wave anisotropy in the Erzincan basin and its relatioship with crustal strain, *J. geophys. Res.*, **102**, 20 373–20 393.

Gaucher, E., 1994. Modele en profondeur et en vitesse du basin d'Erzincan, D.E.A, Institut de Physique du Globe de Paris, Paris.

Hauksson, E. & Haase, J.S., 1997. Three-dimensional V_p and V_p/V_s Velocity Models of the Los Angeles basin and central Transverse Ranges, California, *J. geophys. Res.*, **102**, 5423–5453.

Hempton, M.R. & Dunne, L., 1984. Sedimentation in pull-apart basins: active examples in eastern Turkey, *J. Geol.,* **92**, 513–530.

Hempton, M.R. & Linneman, S.R., 1984. Volcanism in the Erzincan pull-apart basin: age, composition and tectonic significance., *Abstract EOS,* **65**, 84.

Kissling E., 1988. Geotomography with local earthquake data, *Rev. Geophys.*, **26**, 659–698.

Kissling, E., Ellsworth, W.L., Eberhart-Philips, D. & Kradolfer, U., 1994. Initial reference models in local earthquake tomography, *J. geophys. Res.*, **99**, 19 635–19 646.

Klein, F.W., 1978. Hypocenter location program HYPOINVERSE, *Open File Report,* 78–694, US Geological Survey, Boulder, CO.

Olsen, K.B., Archueleta, R.J. & Matarese, J.R., 1995. Three dimensional simulation of a magnitude 7.75 earthquake on the San Andreas Fault, *Science,* **270**, 1628–1632.

Ozgul, N. & Tursucu, A., 1984. Stratigraphy of the Mesozoic carbonate sequence of the Munzur Mountains (eastern Taurides), in *Geology of the Taurus Belt,* pp. 173–180, eds Tekeli, O. & Goncuoglu M., General Directorate and Mineral Research and Exploration, Ankara.

Pinar, A., Honkura, Y. & Kikuchi, M., 1994. Rupture process of the 1992 Erzincan earthquake and its implication for seismotectonics in eastern Turkey, *Geophys. Res. Lett.,* **21**, 1971–1974

Şengör, A.M.C. & Yilmaz, Y., 1987. Tethyan evolution of Turkey: a plate tectonic approach, *Tectonophysics*, **75**, 181–241.

Şengör, A.M.C., Gorur, N. & Saroglu, F., 1985. Strike-slip faulting and related basin formation in zones of tectonic escape: Turkey as a case study, in *Strike-slip Faulting and Basin Formation,* pp. 227–264, eds Biddle, K.T. & Christie-Blick, N., *Society of Econ. Paleont. Min. Spec. Publ.,* Tulsa, OK, USA.

Suzanne, P., Lyberis, N., Chorowics, J., Nurlu, M., Yurur, T. & Kasapoglu, E., 1990. La geometrie de la faille nord anatolienne a partir des images Landsat-MSS, *Bull. Soc. Geol. France,* **8**, 589–599.

Thurber, C.H., 1983. Earthquake location and three-dimensional crustal structure in Coyote Lake area, Central California, *J. geophys. Res.*, **88**, 8226–8236.

Westaway, R. & Arger, J., 2001. Kinematics of the Malatya-Ovacik Fault Zone, *Geodynamica Acta,* **14**, 103–131.